Thermal conductivity in self-assembled $CoFe_2O_4/BiFeO_3$ vertical nanocomposite films

Chen Zhang[1], Samuel C. Huberman[2], Shuai Ning[1], Jonathan Pelliciari[3], Ryan A. Duncan[4], Bolin Liao[2], Alexei Maznev[4], Shuchi Ojha[1], John Freeland[5], Keith A. Nelson[4], Riccardo Comin[3], Gang Chen[2], Caroline A. Ross[1]

[1]Department of Materials Science and Engineering, [2]Department of Mechanical Engineering, [3]Department of Physics and [4]Department of Chemistry, Massachusetts Institute of Technology, Cambridge, MA, United States

[5]Advanced Photon Source, Argonne National Laboratory, Argonne, Illinois 60439, United States

Abstract

The thermal conductivity of self-assembled nanocomposite oxide films consisting of cobalt ferrite (CFO) spinel pillars grown within a single-crystal bismuth ferrite (BFO) perovskite matrix is described as a function of the volume fraction of the spinel. Single phase BFO and CFO had cross-plane thermal conductivities of 1.32 $Wm^{-1}K^{-1}$ and 3.94 $Wm^{-1}K^{-1}$ respectively, and the thermal conductivity of the nanocomposites increased with CFO volume fraction within this range. Steady state gray variance-reduced Monte Carlo simulations also show an increase in thermal conductivity with CFO volume fraction.

The importance of nanoscale heterogeneity in determining thermal transport in materials is well established [1-4]. The thermal transport properties of a heterogeneous system depend on the nature of the materials present, their volume fractions, the structure and geometry of the interfaces, and on the length scale of the modulation with respect to the mean free path of the thermal carriers [5-12]. Interfaces play a significant role, and may be characterized by a thermal conductance arising from their interaction with the phonons and electrons that transport heat through the system [2,13,14]. The thermal transport properties of thin film materials are important in diverse applications including lasers and LEDs, photovoltaics, microelectronic devices, phase change memory, rewritable optical media, and thermoelectric devices.

Materials that consist of two (or more) phases, such as multilayers or superlattices, can be categorized depending whether the mean free path of the thermal carriers is smaller or larger than the characteristic size of the phases in the material. In the former case, the in-plane thermal conductivity parallel to the layers can be treated as the volume-weighted sum of the bulk thermal conductivities of the phases, whereas the cross-plane thermal conductivity perpendicular to the layers can be determined from the sum of the thermal resistance of the two materials plus a contribution from the interfaces [1]. However, for long mean free paths, phonon interference effects become important. For example, superlattice studies have demonstrated a minimum in through-thickness thermal conductivity as a function of the period of the layers, indicating a transition between coherent phonon transport in the low-period regime and incoherent transport for thicker layers at the nm length scale similar to the mean free path of phonons that dominate thermal transport [15-17]. Thermal conductivity parallel to the interfaces is sensitive to specular reflection of phonons from the interfaces, and to interface roughness and other materials properties [12,18-20], leading to anisotropic thermal conductivity.

Thermal transport has been characterized and modeled in a variety of heterogeneous materials with planar interfaces parallel to the substrate, and in materials with randomly oriented interfaces such as nanocrystalline materials [21] or nanoparticles embedded in a matrix [22]. There has been little work on thin film systems with interfaces normal to the film plane, although the thermal conductivity of etched mesoscale structures with interfaces perpendicular to the substrate has been examined [23].

The thermal transport in films with perpendicular interfaces may be conveniently examined by taking advantage of a class of self-assembled two-phase crystalline thin films in which one phase grows as vertical columns embedded in a matrix phase. These structures form spontaneously during codeposition of two immiscible phases such as a spinel and a perovskite. Both phases are epitaxial with the substrate and the interfaces share a common orientation. Notably, the interface strain state is determined primarily by lattice mismatch between the two phases rather than by clamping from the substrate. A range of materials combinations forms vertical nanocomposites [24-30], most commonly spinel-perovskite nanocomposites grown on a perovskite substrate [24], but also nanocomposites containing ZnO or rocksalt structures [27], metal-oxide nanocomposites [28], and even nanocomposites with three components such as $SrTi_xCu_{1-x}O_3$/SrO/Cu [30]. Such structures provide systems with well-defined, densely spaced vertical interfaces, and provide model systems that allow the thermal properties of heterogeneous materials to be quantified.

In this work, we measure the thermal conductivity of spinel/perovskite nanocomposites consisting of pillars of ferrimagnetic $CoFe_2O_4$ (CFO) in a matrix of ferroelectric $BiFeO_3$ (BFO) grown on single crystal (001) $SrTiO_3$ (STO) substrates by pulsed laser deposition. The pillars have a square or rectangular cross-section and the vertical interfaces between the BFO and CFO consist of {110} planes. We use time domain thermoreflectance (TDTR) to measure the thermal conductivity of nanocomposite films in the cross-plane direction normal to the substrate, i.e. parallel to the pillars, as a function of the volume fraction of CFO which determines the density of the interfaces. Steady state gray variance-reduced Monte Carlo simulations of heat transport in the nanocomposite films were carried out. Both the experiment and modeling show an increase in thermal conductivity with CFO volume fraction.

The spinel/perovskite films were grown by codeposition of CFO and BFO from two separate targets using combinatorial pulsed laser deposition (PLD) with a 248 nm wavelength ArF laser as described previously [31]. The STO (001)-oriented substrates were held at a temperature of 750° C. The targets were ablated alternately and the substrate holder was rotated 180° every time the targets were exchanged. Each "layer" of material deposited from either target was less than one monolayer thick (~0.4 nm), ensuring that continuous in-plane multilayers did not form. Instead, diffusion of arriving species on the surface led to the growth of CFO pillars in a BFO matrix. The coordinated motion of the substrate holder and targets during growth led to a set of samples with a range of CFO:BFO ratios.

The area fraction, pillar size and pillar interface length per unit area were obtained by image processing of top-down SEM micrographs. The CFO pillar areas were determined by ImageJ software and the total perimeter was calculated assuming that they each had a square cross-section, yielding the interface density. The volume fraction of CFO was taken as equal to the area fraction of pillars in the SEM images on the assumption that the pillars have vertical facets, as observed in prior work [32]. For each image a threshold pillar area was set such that small pillars or features of order 5 nm diameter and below were excluded from the analysis.

Magnetic hysteresis of the samples was measured using a vibrating sample magnetometer (ADE VSM) in fields up to 10 kOe. X-ray absorption spectroscopy (XAS) and x-ray magnetic circular dichroism (XMCD) were measured at the Advanced Photon Source at Argonne National Laboratory using beamline 4-ID-C. A magnetic field of 3.36 kOe was applied normal to the film plane and XAS was measured in total electron yield (TEY) and total fluorescence yield (TFY) modes. The cross-plane thermal conductivity was measured by TDTR [33-35] at 300 K and 220 K. Aluminum layers with thickness of ~85 nm were deposited on the nanocomposite films to serve as a transducer. By measuring the time-dependent reflectivity of the metallic Al overlayer after heating with a pulsed pump laser (wavelength 400 nm, pulse width 200 fs, spot size 50 μm) using a time-delayed probe laser (wavelength 800 nm, modulation frequencies 3, 6, 9, 12 MHz), the thermal transport properties in the underlying thin film were extracted by fitting to a three-layer heat diffusion equation for the cooling of the sample [34]. The layer structure consists of the Al film, the nanocomposite film, and a finite thermal interface conductance separating them. The parameters used as the input of the fitting are given in **Table I.**

SEM images of four nanocomposite samples are illustrated in **Figure 1.** The thickness of each sample was 51 nm, as indicated by the XRR (X-ray reflectivity) measurement and fitting, **Figure 2a**. X-ray diffraction (XRD), **Figure 2b**, shows the presence of both spinel and perovskite peaks consistent with the phase-separated morphology, with the CFO peak intensity increasing with volume fraction. Prior work has shown that the BFO grows with cube-on-cube epitaxy on the STO, i.e. $<001>_{BFO}$ is parallel to $<001>_{STO}$. The CFO is also cube-on-cube epitaxial with the STO (its lattice parameter is close to twice that of the BFO and STO) and grows as rectangular pillars with {110} vertical facets within the BFO matrix. The CFO pillars are terminated with four {111} facets and a top (001) facet [29].

Figure 2c shows the average pillar edge length and the interface density as a function of the volume fraction of CFO, which varied from 6.3% to 43.6%. The interface density, found from the total perimeter of the pillars, initially increased with increasing volume fraction, but was almost the same for the two samples with highest volume fraction. The average pillar edge length was similar for the two samples with lowest volume fraction, but then increased with volume fraction. The trends suggest that for small CFO flux there is an increasing probability of pillar nucleation with increasing flux, but above a certain volume fraction (here above ~12%) additional flux contributes to increasing the size of the pillars rather than nucleating new ones. There is considerable distribution of pillar sizes and spacings in all the samples, but the average spacing is the order of 50 nm and average pillar diameters are 12-22 nm.

The magnetic hysteresis loops of one of the samples is shown in **Figure 3(a)**. Other samples showed similar loop shapes. The magnetic hysteresis originates from the CFO pillars, and the BFO, a canted antiferromagnet, contributes negligibly. All the samples show similar saturation magnetization normalized by CFO volume fraction, of order 50-60 emu cm^{-3}. The magnetization is low compared to that of bulk CFO (~400 emu cm^{-3} [36]), which is attributed to the non-ideal stoichiometry of the CFO pillars. Growth of single phase CFO films from the same target under similar PLD conditions led to excess Co such that Co:Fe ~ 1.4:2 instead of the stoichiometric ratio of 1:2. As shown in **Figure 3(b)**, increasing the Fe content of single-phase CFO by combinatorial deposition from CFO and Fe_3O_4 targets led to an increase in the magnetization of the film. However, the nanocomposites were not deposited with additional Fe_3O_4 and the pillars are therefore assumed to approximate the $Co_{1.2}Fe_{1.8}O_4$ composition obtained from the CFO target corresponding to sample 1 of Figure 3(b).

Both Co^{2+} and Co^{3+} have a preference for the octahedral (O_h) sites in spinel, but the degree of inversion (site occupancy) of the spinel can depend on its preparation conditions [37,38]. The magnetic moments on the tetrahedral (T_d) and octahedral sites are coupled antiferromagnetically, so for stoichiometric $CoFe_2O_4$ without oxygen deficiency, which can be written $[Fe^{3+}]_{tet}[Fe^{3+}, Co^{2+}]_{oct}O_4$, the net magnetic moment is due only to the Co^{2+} O_h because the Fe^{3+} moments cancel out. For the $Co_{1.2}Fe_{1.8}O_4$ spinel, which can be written $[Fe^{3+}]_{tet}[Fe^{3+}_{0.8}, Co^{3+}_{0.2}, Co^{2+}_{1.0}]_{oct}O_4$, the Fe magnetic moments no longer compensate each other. The net magnetic moment is then expected to be lower than for $CoFe_2O_4$.

The XAS and XMCD results (**Figure 4**) of two nanocomposites, which were grown at a different time from those of Figure 1 but with similar growth conditions, show that both Co and Fe have a non-zero net magnetic moment as displayed by the presence of dichroism in Fig. 4b and d. By comparing the profile of the Fe XAS (Fig. 4a) with prior reports, we find that Fe is primarily in the Fe^{2+} and Fe^{3+} ionic states, and while we cannot rule out a contribution from Fe^{3+} in the BFO, which has a weak magnetism due to antiferromagnetic canting, the latter is too small to account for the Fe XMCD [39-42]. The XAS of cobalt reported in Fig. 4c indicates a mixed oxidation state comprising mainly Co^{2+} and Co^{3+}. This observation is consistent with an imbalance between Fe site from the O_h and T_d sublattices, as expected from the excess Co present at the octahedral sites. Indeed, the XMCD lineshape in Fig. 4b reveals the presence of Fe^{2+} and Fe^{3+} O_h and Fe^{3+} T_d [39-42]. The XMCD signal observed on the Co site indicates that the direction of the spins is parallel to Fe^{2+}/Fe^{3+} O_h and opposite to the Fe^{3+} T_d, which further corroborates the hypothesis of an inverse spinel.

The magnetization and other properties such as magnetocrystalline anisotropy and magnetostriction are sensitive to the chemical distribution and valence states of the cations on the octahedral and tetrahedral sites. Cation off-stoichiometry in CFO is known to lower the magnetization, both for Co-rich [36] and Co-deficient [43] compositions, and can lead to formation of secondary phases such as (antiferromagnetic) rocksalt structures. Excess Co also dramatically reduces the magnetostriction in bulk CFO [36]. In the nanocomposite, there also exists the possibility of cation exchange with the BFO, although prior work did not show significant Co incorporation into BFO [32].

The loops for the nanocomposites for out-of-plane field and in-plane field are similar indicating less magnetic anisotropy than for previously reported nanocomposites [31]. The anisotropy originates from magnetoelastic anisotropy due to the out-of-plane compressive strain state of the CFO caused by its lattice mismatch with the BFO at the vertical interfaces, and shape anisotropy from the pillars. Magnetocrystalline anisotropy does not contribute to the difference between the in-plane (field in the [100] direction) and out-of-plane (field in the [001] direction) loops. The low anisotropy of the samples is attributed to two factors. First, the lower magnetostriction of the off-stoichiometric CFO reduces the contribution of magnetoelastic anisotropy. Second, the low film thickness limits the pillar aspect ratio (height/diameter) which in combination with the low magnetic moment reduces the shape anisotropy.

Figure 5a shows the thermal conductivity extracted from TDTR of the nanocomposites plotted vs. CFO volume fraction. We reported thermal conductivity of 1.32 $Wm^{-1}K^{-1}$ for single-phase BFO films, [44], and we measured a conductivity of 3.7 – 3.9 $Wm^{-1}K^{-1}$ for single-phase CFO films grown on (110) STO with Co:Fe stoichiometry of 1:2, **Figure 5b**. An interesting result for the single-phase CFO is that the thermal conductivity had a small dependence on the magnetization state, with the conductivity of films at remanence after saturation approximately 5% smaller than that of AC-demagnetized films, Figure 5b.

For the nanocomposites, the thermal conductivity scales approximately linearly with CFO volume fraction, increasing by a factor of ~2 in the range of 6.3 – 43.6% vol. CFO. The interface density appears to be less significant, since the two highest volume fraction samples have similar interface densities but different thermal conductivities. The thermal conductivity at 220 K is slightly higher or similar to that measured at 300 K. An increase in thermal conductivity with decreasing temperature is expected in single crystals due to the reduction in phonon-phonon scattering and increase of the mean free path of the phonons at low temperature. The heterogeneous nature of the nanocomposite is assumed to limit the mean free path and therefore the amount of enhancement in thermal conductivity as the temperature decreases.

The linear increase in thermal conductivity with CFO volume fraction is reproduced by modeling, described below. However, comparing to the single-phase films, even the lowest fraction of CFO yielded a significant increase in thermal conductivity over that of single-phase BFO, and the thermal conductivity of the nanocomposites with 43.6% CFO was close to that measured for single-phase CFO. This may indicate that the single-phase film properties are not identical to those of the same material in the nanocomposite, due to differences in strain state [45] or in the composition of the CFO.

To simulate heat transport in the BFO/CFO nanocomposite films, steady state gray variance-reduced Monte Carlo simulations [46,47] at room temperature were performed, **Figure 5c**. The hot side temperature was fixed at 301K and the cold side temperature was fixed at 300K. Film thickness was 42nm. Two sets of gray properties were manipulated to achieve the pure values of BFO and CFO. The domain consisted of a matrix and a single centered pillar, where the square pillar was fixed to have sides of length 12 nm. The remaining matrix dimensions were set to maintain the desired volume fraction. The probability of transmission between pillar and matrix was fixed at 0.5. The model predicts an approxmately linear increase in thermal conductivity with CFO volume fraction, consistent with the experimental data. This suggests that in the nanocomposite, the averaged contributions of the two phases, rather than contributions from the interfaces, govern the cross-plane thermal conductivity.

Transient thermal grating (TTG) spectroscopy was used to characterize the in-plane thermal conductivity, perpendicular to the pillar axis, in which two interfering laser beams produce a spatially-modulated thermal profile in an absorbing layer whose decay is measured by the diffraction of a probe beam [48,49]. However, based on modeling of the effect of film thickness and on the bulk thermal conductivities of STO and BFO, the analysis was insensitive to variations in the film in-plane thermal conductivity due to the dominant effect of the substrate. This precluded identification of a trend in the in-plane thermal conductivity of the samples.

In summary, self-assembled BFO/CFO vertical nanocomposite films with volume fractions of CFO in the range 6.3 – 43.6% were grown via combinatorial pulsed laser deposition. The cross-plane thermal conductivity, in which the heat flow is parallel to the BFO/CFO interfaces, increased approximately linearly with CFO content from 2.25 $Wm^{-1}K^{-1}$ to 3.94 $Wm^{-1}K^{-1}$ at room temperature, between the thermal conductivities of single-phase BFO and CFO. Steady state gray variance-reduced Monte Carlo simulations at room temperature reproduced the increasing thermal conductivity with CFO volume fraction.

Acknowledgement

This work was supported as part of the Solid-State Solar-Thermal Energy Conversion Center (S3TEC), an Energy Frontier Research Center funded by the U.S. Department of Energy, Office of Science, Basic Energy Sciences under Award # DE-SC0001299. This work made use of shared experimental facilities of CMSE, supported under NSF DMR1419807.

References

1 David G. Cahill, Wayne K. Ford, Kenneth E. Goodson, Gerald D. Mahan, Arun Majumdar, Humphrey J. Maris, Roberto Merlin, Simon R. Phillpot, Nanoscale thermal transport, J. Appl. Phys., Vol. 93, No. 2, 15 January 2003, 793-818

2 E. T. Swartz, R. O. Pohl, Thermal boundary resistance, Reviews of Modern Physics, Vol. 61, No. 3, July 1989 605-668

3 P.E. Hopkins, Thermal Transport across Solid Interfaces with Nanoscale Imperfections: Effects of Roughness, Disorder, Dislocations, and Bonding on Thermal Boundary Conductance, ISRN Mechanical Engineering Volume 2013 (2013), Article ID 682586, 19 pages, http://dx.doi.org/10.1155/2013/682586

4 Ashutosh Giri, Jeffrey L. Braun, and Patrick E. Hopkins, Effect of crystalline/amorphous interfaces on thermal transport across confined thin films and superlattices, J Appl Phys 119, 235305 (2016)

5 G. Chen, Thermal conductivity and ballistic-phonon transport in the cross-plane direction of superlattices, Phys. Rev. B 57, 14958 – Published 15 June 1998

6 J. Ravichandran: Thermoelectric and thermal transport properties of complex oxide thin films, heterostructures and superlattices, J. Mater. Res., Vol. 32, No. 1, Jan 13, 2017 183-203

7 Dong-Wook Oh, Jayakanth Ravichandran, Chen-Wei Liang, Wolter Siemons, Bharat Jalan, Charles M. Brooks, Mark Huijben, Darrell G. Schlom, Susanne Stemmer, Lane W. Martin, Arun Majumdar, Ramamoorthy Ramesh, and David G. Cahill, Thermal conductivity as a metric for the crystalline quality of SrTiO3 epitaxial layers, Appl. Phys.

Lett. 98, 221904 (2011)

8 Maria N. Luckyanova, Jivtesh Garg, Keivan Esfarjani, Adam Jandl, Mayank T. Bulsara, Aaron J. Schmidt, Austin J. Minnich, Shuo Chen, Mildred S. Dresselhaus, Zhifeng Ren, Eugene A. Fitzgerald, Gang Chen, Coherent phonon heat conduction in superlattices. Science 338, 936–939 (2012)

9 Y. K. Koh, Y. Cao, D.G. Cahill, and D. Jena, Heat-transport mechanisms in superlattices. Adv. Funct. Mater. 19, 610–615 (2009)

10 V. Narayanamurti, H. L. Stormer, M. A. Chin, A. C. Gossard and W. Wiegmann, Selective Transmission of High-Frequency Phonons by a Superlattice: The "Dielectric" Phonon Filter, Phys. Rev. Lett. 43 (1979) 2012-2016

11 G. Chen, Size and interface effects on thermal conductivity of superlattices and periodic thin-film structures. J. Heat Transf. 119, 220–229 (1997).

12 G. Chen, T Zeng, T. Borca-Tasiuc, D Song, Phonon engineering in nanostructures for solid-state energy conversion, Mater. Sci. Eng. A, 292(2) 2000, Pages 155–161

13 Ruxandra M. Costescu, Marcel A. Wall, and David G. Cahill, Thermal conductance of epitaxial interfaces, Phys. Rev. B 67, 054302 (2003)

14 Ajit K. Roy, Barry L. Farmer, Vikas Varshney, Sangwook Sihn, Jonghoon Lee, and Sabyasachi Ganguli, Importance of Interfaces in Governing Thermal Transport in Composite Materials: Modeling and Experimental Perspectives, ACS Appl. Mater. Interfaces 2012, 4, 545−563

15 J. Ravichandran, A.K. Yadav, R. Cheaito, P.B. Rossen, A. Soukiassian, S.J. Suresha, J.C. Duda, B.M. Foley, C-H. Lee, Y. Zhu, A.W. Lichtenberger, J.E. Moore, D.A. Muller, D.G. Schlom, P.E. Hopkins, A. Majumdar, R. Ramesh, and M.A. Zurbuchen: Crossover from incoherent to coherent phonon scattering in epitaxial oxide superlattices. Nat. Mater. 13, 168 (2014).

16 A. Chernatynskiy, R. W. Grimes, M. A. Zurbuchen, D. R. Clarke, and S. R. Phillpot, Crossover in thermal transport properties of natural, perovskite-structured superlattices. Appl. Phys. Lett. 95, 161906 (2009).

17. M. V. Simkin and G. D. Mahan, Minimum Thermal Conductivity of Superlattices, Phys. Rev. Lett. 84, 927 2000

18. Konstantinos Termentzidis, Patrice Chantrenne, and Pawel Keblinski, Nonequilibrium molecular dynamics simulation of the in-plane thermal conductivity of superlattices with rough interfaces, Phys. Rev. B 79, 214307 2009

19. Xinjiang Wang & Baoling Huang, Computational Study of In-Plane Phonon Transport in Si Thin Films, Sci. Rep. 4 : 6399 2014

20. Xin-Gang Liang, Bo Shi, Two-dimensional molecular dynamics simulation of the thermal conductance of superlattices, Materials Science and Engineering A292 (2000) 198–202

21. Sabah K. Bux, Richard G. Blair, Pawan K. Gogna, Hohyun Lee, Gang Chen, Mildred S. Dresselhaus, Richard B. Kaner, and Jean-Pierre Fleurial, Nanostructured Bulk

Silicon as an Effective Thermoelectric Material, Adv. Funct. Mater. 2009, 19, 2445–2452

22. Biswas K, He J, Zhang Q, Wang G, Uher C, et al.. Strained endotaxial nanostructures with high thermoelectric figure of merit. *Nat. Chem.* 3 160–66 2011

23. Konstantinos Termentzidis, Jayalakshmi Parasuraman, Carolina Abs Da Cruz, Samy Merabia, Dan Angelescu, Frédéric Marty, Tarik Bourouina, Xavier Kleber, Patrice Chantrenne and Philippe Basset, Thermal conductivity and thermal boundary resistance of nanostructures, Nanoscale Research Letters 2011, 6:288

24. Zheng, H.; Wang, J.; Lofland, S.; Ma, Z.; Mohaddes-Ardabili, L.; Zhao, T.; Salamanca-Riba, L.; Shinde, S.; Ogale, S.; Bai, F., Multiferroic $BaTiO_3$-$CoFe_2O_4$ nanostructures. *Science* 2004, 303, 661-663.

25. Chen, A.; Bi, Z.; Jia, Q.; MacManus-Driscoll, J. L.; Wang, H., Microstructure, vertical strain control and tunable functionalities in self-assembled, vertically aligned nanocomposite thin films. *Acta Materialia* 2013, 61, 2783-2792.

26. Zhang, W.; Chen, A.; Bi, Z.; Jia, Q.; MacManus-Driscoll, J. L.; Wang, H., Interfacial coupling in heteroepitaxial vertically aligned nanocomposite thin films: From lateral to vertical control. *Current Opinion in Solid State and Materials Science* 2014, 18, 6-18.

27. Chen, A.; Bi, Z.; Tsai, C. F.; Lee, J.; Su, Q.; Zhang, X.; Jia, Q.; MacManus-Driscoll, J. L.; Wang, H., Tunable Low-Field Magnetoresistance in (La0.7Sr$_{0.3}$MnO3)$_{0.5}$: (ZnO)$_{0.5}$ Self-Assembled Vertically Aligned Nanocomposite Thin Films. *Advanced Functional Materials* 2011, 21, 2423-2429.

28. L. Mohaddes-Ardabili, H. Zheng, S. B. Ogale, B. Hannoyer, W. Tian, J. Wang, S. E. Lofland, S. R. Shinde, T. Zhao, Y. Jia, L. Salamanca-Riba, D. G. Schlom, M. Wuttig & R. Ramesh, Self-assembled single-crystal ferromagnetic iron nanowires formed by decomposition, Nature Materials 3, 533 - 538 (2004)

29. Haimei Zheng, Qian Zhan, Florin Zavaliche, Matt Sherburne, Florian Straub, Maria P. Cruz, Long-Qing Chen, Uli Dahmen, and R. Ramesh, Controlling Self-Assembled Perovskite−Spinel Nanostructures, *Nano Lett.*, 2006, 6 (7), pp 1401–1407

30. Dong Hun Kim, Xue Yin Sun, Nicolas M. Aimon, Jae Jin Ki , Michael J. Campion, Harry L. Tuller, Lior Kornblum, Fred J. Walker, Charles H. Ahn, and Caroline A. Ross, A Three Component Self-Assembled Epitaxial Nanocomposite Thin Film, Adv. Funct. Mater. 2015, *25*, 3091–3100

31. Nicolas M. Aimon, Dong Hun Kim, Hong Kyoon Choi, and C. A. Ross, Deposition of epitaxial BiFeO3/CoFe2O4 nanocomposites on (001) $SrTiO_3$ by combinatorial pulsed laser deposition, Appl. Phys. Lett. 2012, 100, 092901

32. Nicolas M. Aimon, Hong Kyoon Choi, Xue Yin Sun, Dong Hun Kim, and Caroline A. Ross, Templated Self-Assembly of Functional Oxide Nanocomposites, Adv. Mater. 2014, 26, 3063–3067

33. Capinski, W. S.; Maris, H. J. Improved apparatus for picosecond pump-and-probe optical measurements, Rev. Sci. Instrum. 1996, 67, 2720-2726.

34. Cahill, D. G.; Goodson, K.; Majumdar, A. Thermometry and Thermal Transport in Micro/Nanoscale Solid-State Devices and Structures, J. Heat Trans. 2002, 124, 223-241.

35. Schmidt, A. J.; Chen, X.; Chen, G. Pulse accumulation, radial heat conduction, and anisotropic thermal conductivity in pump-probe transient thermoreflectance, Rev. Sci. Instrum. 2008, 79, 114902.

36. I.C. Nlebedim, A.J. Moses,D.C. Jiles, Non-stoichiometric cobalt ferrite, $Co_xFe_{3-x}O_4$ (x=1.0 to 2.0): Structural, magnetic and magnetoelastic properties, Journal of Magnetism and Magnetic Materials, 343, October 2013, Pages 49-54

37. Vaingankar, A.S., Khasbardar, B.V., Patil, R.N., X-ray spectroscopic study of cobalt ferrite, Journal of Physics F: Metal Physics 10, 1980, 1615-1619

38. G. A. Sawatzky, F. Van Der Woude, and A. H. Morrish, Mössbauer study of several ferrimagnetic spinels, Phys. Rev. 187, 747 1969

39. Y. K. Wakabayashi, Y. Nonaka, Y. Takeda, S. Sakamoto, K. Ikeda, Z. Chi, G. Shibata, A. Tanaka, Y. Saitoh, H. Yamagami, M. Tanaka, A. Fujimori, and R. Nakane, Electronic structure and magnetic properties of magnetically dead layers in epitaxial CoFe2O4/Al2O3 /Si(111) films studied by x-ray magnetic circular dichroism, Phys Rev B 96, 104410;

40. E. Pellegrin, M. Hagelstein, S. Doyle, H. O. Moser, J. Fuchs, D. Vollath, S. Schuppler, M. A. James, S. S. Saxena, L. Niesen, O. Rogojanu, G. A. Sawatzky, Ferrero, M. Borowski, O. Tjernberg, and N. B. Brookes, Characterization of Nanocrystalline g-Fe 2O3 with Synchrotron Radiation Techniques Phys. Stat. Sol (b) 215,797 (1999);

41. R.A.D. Pattrick, G. van der Laan, C. M. B. Henderson, P. Kuiper, E. Dudzik 2 , and D. J. Vaughan Cation site occupancy in spinel ferrites studied by X-ray magnetic circular dichroism: developing a method for mineralogists Eur. J. Mineral. 2002, 14, 109;

42. C. I. Pearce, C. M. B. Henderson, R.A.D. Pattrick, G. van der Laan , and D. J. Vaughan, Direct determination of cation site occupancies in natural ferrite spinels by L 2,3 X-ray absorption spectroscopy and X-ray magnetic circular dichroism, American Mineralogist, Volume 91, 880 (2006)].

43. I. C. Nlebedim, J. E. Snyder, A. J. Moses, and D. C. Jiles, Effect of deviation from stoichiometric composition on structural and magnetic properties of cobalt ferrite, CoxFe3-xO4 (x = 0.2 to 1.0), Journal of Applied Physics 111, 07D704 (2012)

44. S. Ning, S. C. Huberman, C. Zhang, Z. Zhang, G. Chen, and C. A. Ross, Structure and Polarization Dependence of the Thermal Conductivity of BiFeO3 Thin Films, Physical Review Applied 8, 054049 (2017)

45. X. Li, K. Maute, M. L. Dunn, and R. Yang, Strain effects on the thermal conductivity of nanostructures, Phys. Rev. B 81, 245318 (2010).

46. Peraud, J-P M., Hadjiconstantinou, N.G., Efficient simulation of multidimensional phonon transport using energy-based variance –reduced Monte Carlo formulations. Phys. Rev. B 84, 205331 (2011).

47. Peraud, J-P M., Hadjiconstantinou, N.G., An alternative approach to efficient simulation of micro/nanoscale phonon transport. Appl. Phys. Lett. 101, 153144 (2012).

48. Rogers J A, Maznev A A, Banet M J and Nelson K A, Optical Generation and Characterization of Acoustic Waves in Thin Films: Fundamentals and Applications, Annu. Rev. Mater. Sci. 30 117 (2000)

49. O.W. Käding, H. Skurk, A.A. Maznev, E. Matthias, Transient thermal gratings at surfaces for thermal characterization of bulk materials and thin films, Appl. Phys. A (1995) 61: 253.

Table I. The parameters used as input in the fitting of a three-layer heat diffusion equation

	Thermal conductivity (W/m·K)	Volumetric heat capacity C, 300 K ($J/m^3 \cdot K$)	Layer Thickness
Al	236.8	2.490×10^6	85 nm
CFO_xBFO_{1-x}	κ	$xC_{CFO} + (1-x)C_{BFO}$ ($C_{CFO}=3.445\times10^6$, $C_{BFO}=3.074\times10^6$)	50 nm
STO	11.2	2.617×10^6	500 μm

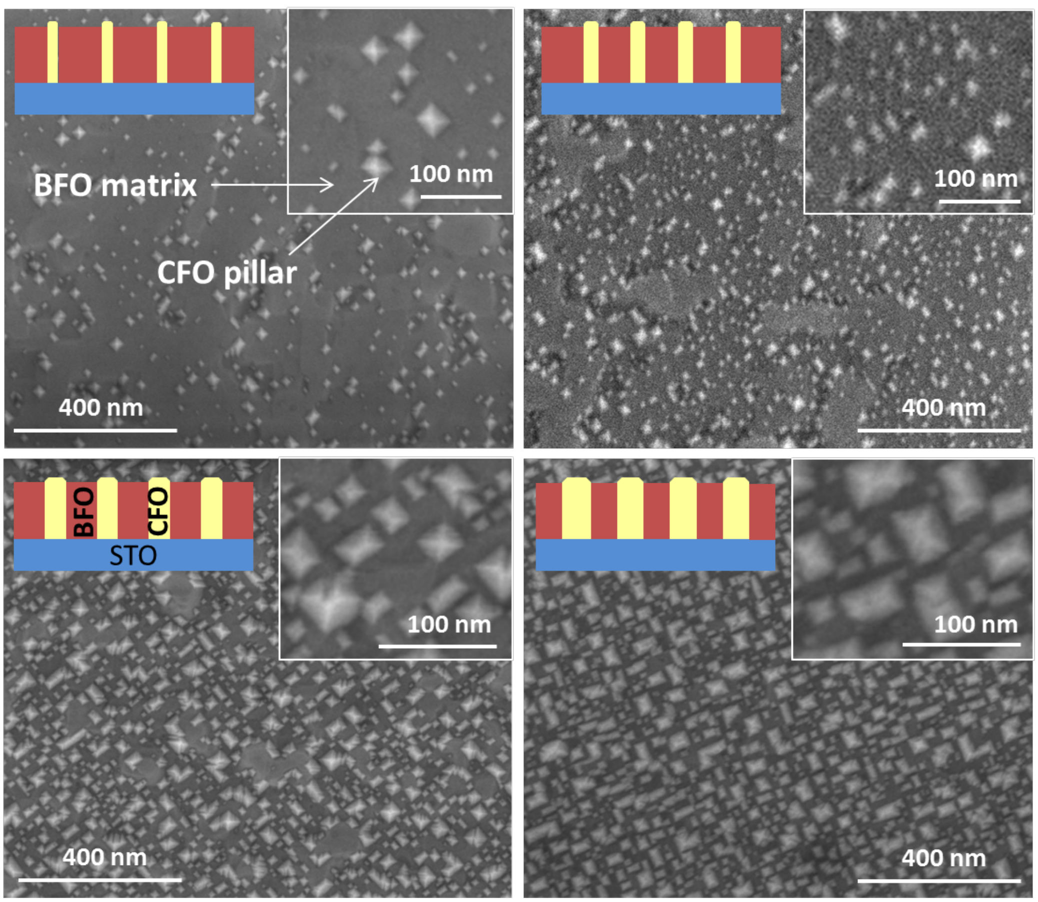

Figure 1 SEM top view images of four BFO/CFO nanocomposites of increasing CFO volume fraction. The left insets show the structure schematically and the right insets show higher magnification images.

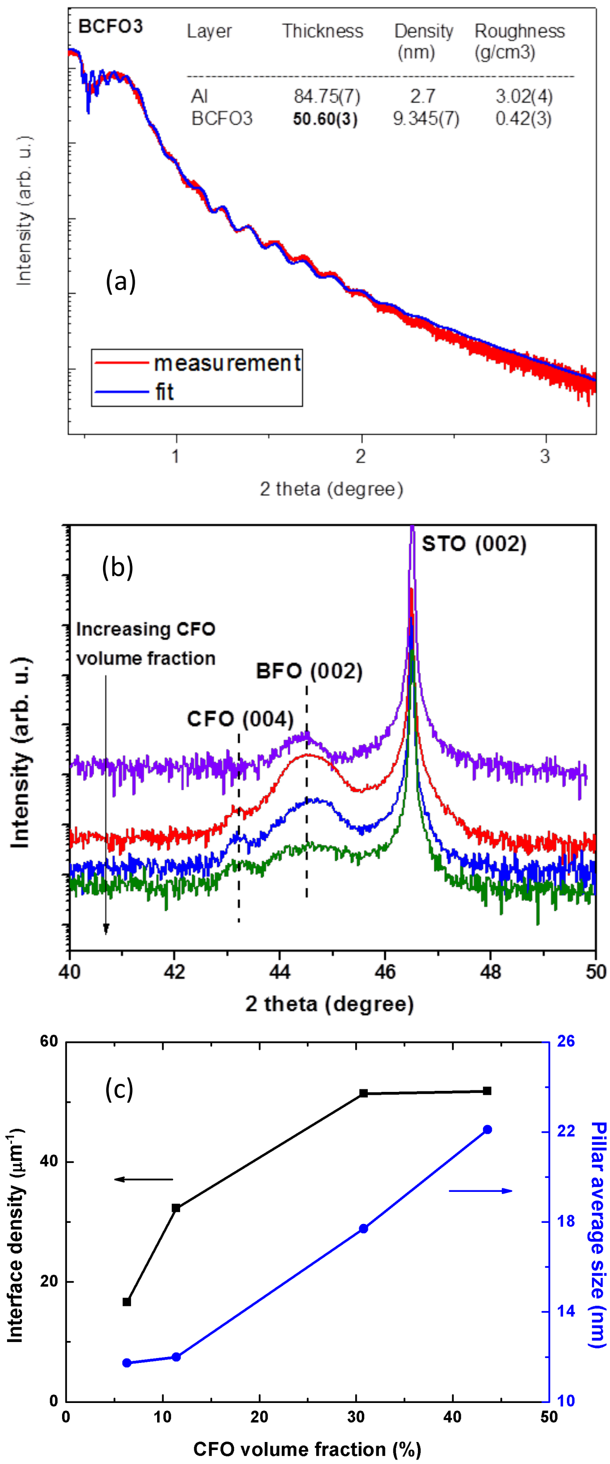

Figure 2 (a) XRR thickness measurement and fitting of the nanocomposite film and Al overlayer. (b) ω–2θ scans of the nanocomposites showing the CFO, BFO and STO peaks. (c) Pillar size and interface density as a function of the volume fraction of CFO, based on SEM image analysis.

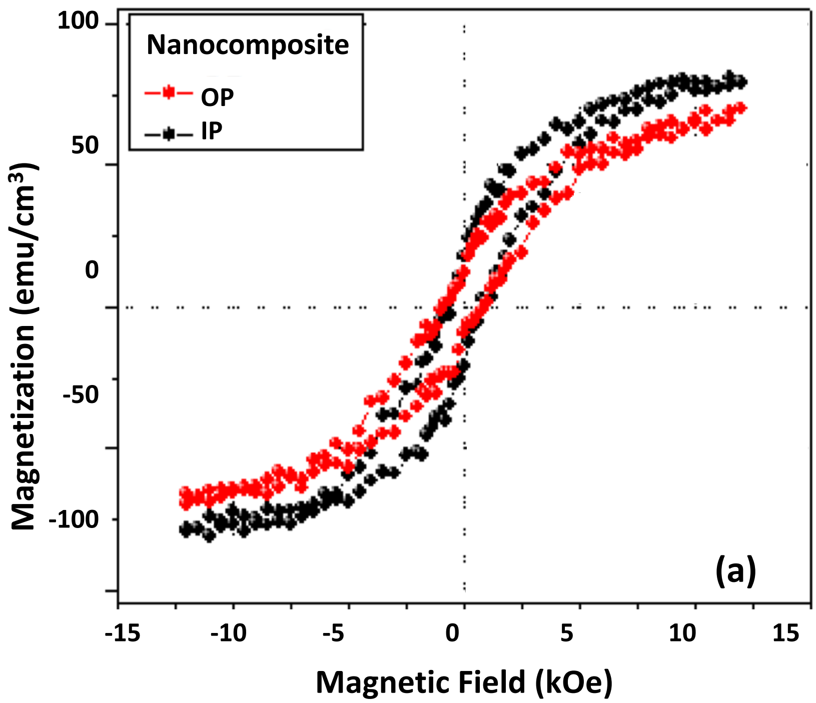

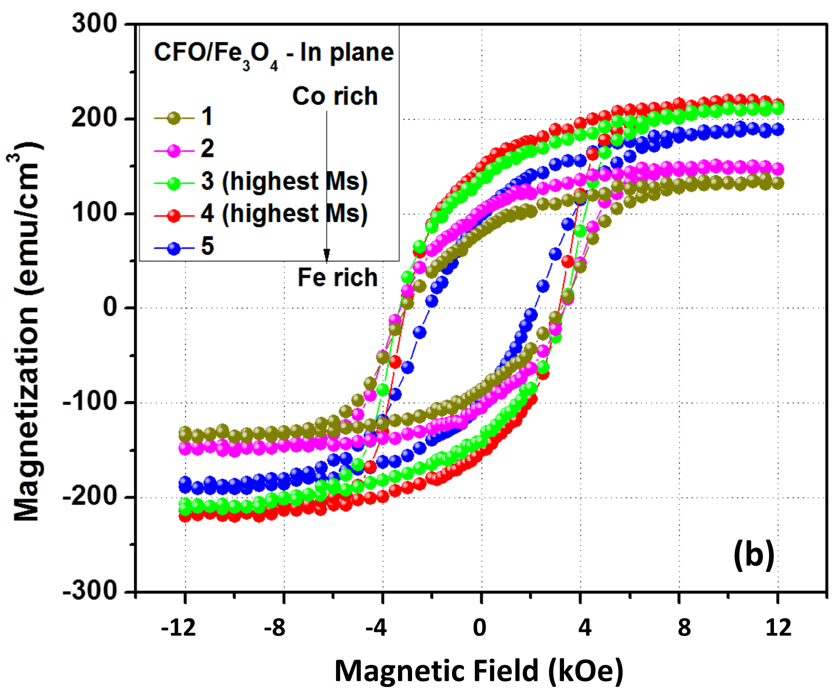

Figure 3. (a) VSM hysteresis loops of the nanocomposite corresponding to the bottom left sample in Figure 1, normalized to the CFO volume, measured with out-of-plane (OP) and in-plane (IP) field. (b) IP hysteresis loops of CFO grown with increasing amounts of codeposited Fe_3O_4. Sample 4 has the composition closest to stoichiometric CFO.

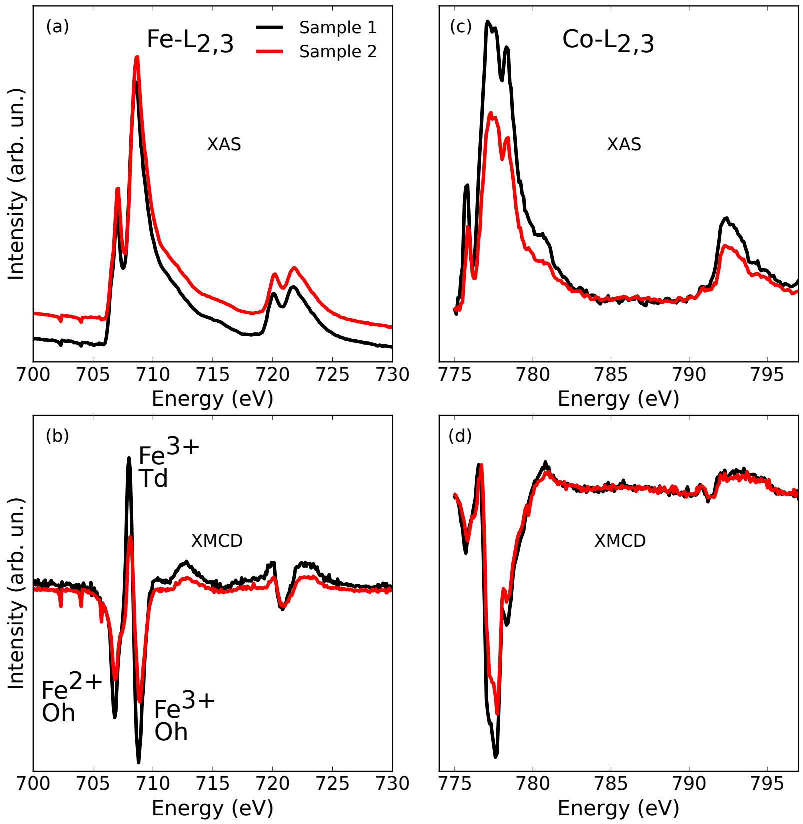

Figure 4. (a,c) XAS and (b,d) XMCD of BFO-CFO nanocomposites measured in TEY mode, for (a,b) Fe and (c,d) Co. Red and black data represent measurements from two different samples.

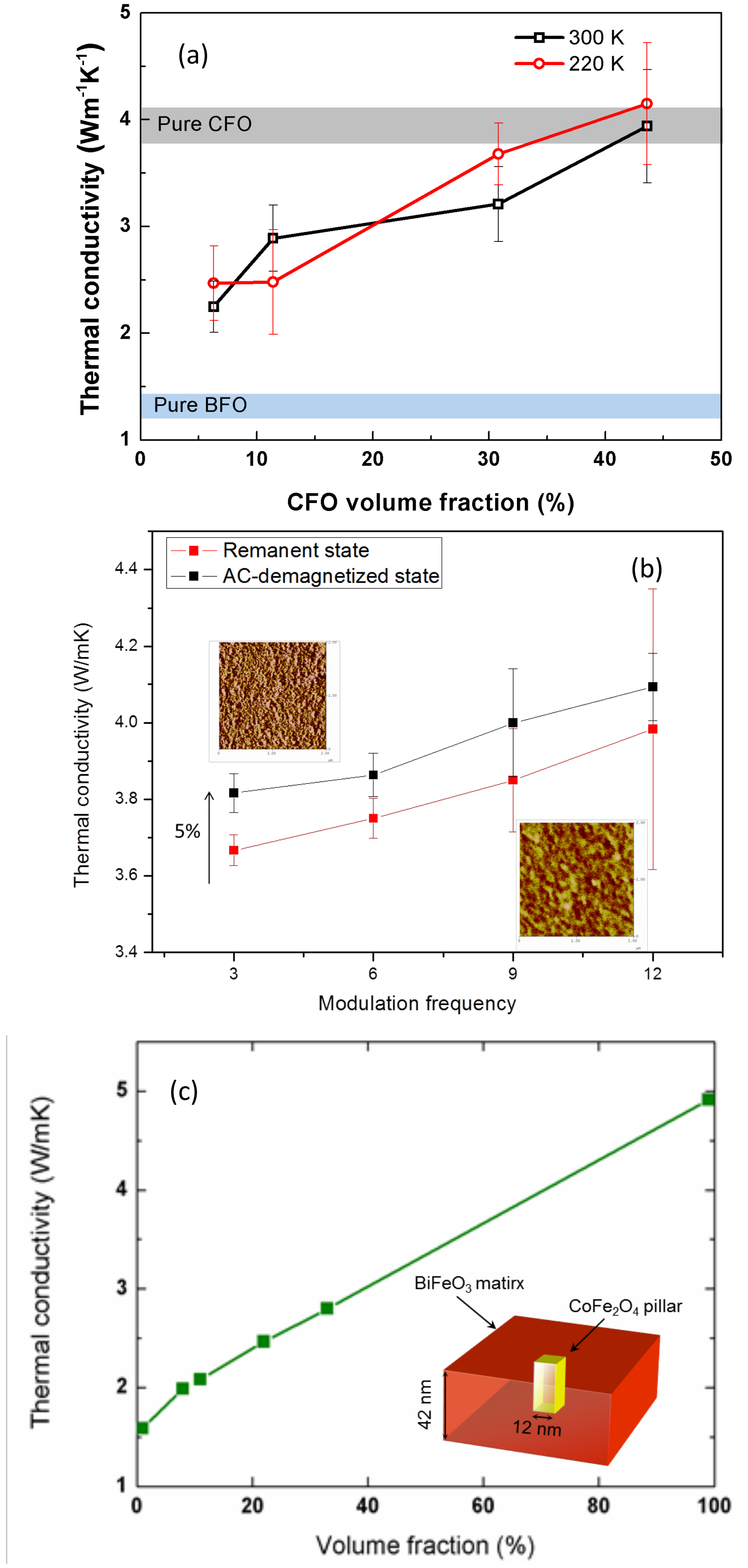
(a)
300 K
220 K
Pure CFO
Pure BFO
Thermal conductivity (Wm-1K-1)
CFO volume fraction (%)
1
2
3
4
5
0
10
20
30
40
50
(b)
Remanent state
AC-demagnetized state
5%
Thermal conductivity (W/mK)
Modulation frequency
3.4
3.6
3.8
4.0
4.2
4.4
3
6
9
12
(c)
BiFeO3 matirx
CoFe2O4 pillar
42 nm
12 nm
Thermal conductivity (W/mK)
Volume fraction (%)
1
2
3
4
5
0
20
40
60
80
100

Figure 5 (a) Dependence of cross-plane thermal conductivity on CFO volume fraction at 220 K and 300 K measurement temperature; (b) Thermal conductivity of a CFO single phase film grown on STO (110) measured at different modulation frequencies, both in a dc-remanent state and after ac-demagnetization. The insets are 2 μm x 2 μm magnetic field microscope images of the sample showing finer, higher contrast domain patterns in the ac-demagnetized state. (c) Simulated cross-plane thermal conductivity versus CFO volume fraction. Inset: Schematics of the simplified geometry used in the steady state gray variance-reduced Monte Carlo simulation.